

Enhanced second-order sideband generation and slow-fast light via coupled opto- and magnomechanical microspheres

Abdul Wahab,¹ Muqaddar Abbas,² Xiaosen Yang,^{1,*} Yuee Xie,^{1,3} and Yuanping Chen^{1,3,†}

¹*Department of Physics, Jiangsu University, Zhenjiang, 212013, China*

²*Ministry of Education Key Laboratory for Nonequilibrium Synthesis and Modulation of Condensed Matter, Shaanxi Province Key Laboratory of Quantum Information and Quantum Optoelectronic Devices,*

School of Physics, Xi'an Jiaotong University, Xi'an 710049, China

³*Quantum Sensing and Agricultural Intelligence Detection Engineering Center of Jiangsu Province, Zhenjiang, Jiangsu, 212013, P. R. China*

(Dated: December 20, 2024)

In this research, we investigate second-order sideband generation (SSG) and slow-fast light using a hybrid system comprised of two coupled opto- and magnomechanical microspheres, namely a YIG sphere and a silica sphere. The YIG sphere hosts a magnon mode and a vibration mode induced by magnetostriction, whereas the silica sphere has an optical whispering gallery mode and a mechanical mode coupled via optomechanical interaction. The mechanical modes of both spheres are close in frequency and are coherently coupled by the straightway physical contact between the two microspheres. We use a perturbation approach to solve the Heisenberg-Langevin equations, offering an analytical framework for transmission rate and SSG. Using experimentally feasible settings, we demonstrate that the transmission rate and SSG are strongly dependent on the magnomechanical, optomechanical, and mechanics mechanics coupling strengths (MMCS) between the two microspheres. The numerical results show that increasing the MMCS can enhance both the transmission rate and SSG efficiency, resulting in gain within our system. Our findings, in particular, reveal that the efficiency of the SSG can be effectively controlled by cavity detuning, decay rate, and pump power. Notably, our findings suggest that modifying the system parameters can alter the group delay, thereby regulating the transition between fast and slow light propagation, and vice versa. Our protocol provides guidelines for manipulating nonlinear optical properties and controlling light propagation, with applications including optical switching, information storage, and precise measurement of weak signals.

I. Introduction

Cavity magnomechanics (CMM) [1, 2], which involves coupling a microwave (MW) cavity with a ferrimagnetic crystal such as yttrium iron garnet (YIG), has emerged as a rapidly expanding field with significant applications in contemporary quantum technologies [3, 4]. This field opens new avenues for investigating the interactions between magnon, cavity, and phonon modes [5, 6]. Magnetic materials, particularly YIG, are noteworthy due to their high spin density, long coherence times, and strong spin-spin exchange interactions, offering a novel platform for cavity optomagnonics [7–10]. The unique dynamics of YIG enable promising applications, including long-time memory [11, 12], microwave-to-optical conversion [13, 14], magnon-induced nonreciprocity [15, 16], enhanced tripartite interactions [17], quantum entanglement [18, 19], and precision measurements [20–22], to name a few.

Simultaneously, the shape distortion of the YIG structure during magnetization induces a nonlinear interaction between the phonon and magnon modes [23]. Experimentally, strong and ultrastrong couplings between magnons and microwave photons have been achieved through magnetic dipole interaction [11, 24], providing

a unique platform for exploring various quantum effects [25–32]. In addition, CMM, like cavity optomechanics, has been proposed and demonstrated experimentally, where magnon-phonon interaction is introduced through magnetostrictive force resulting in magnomechanically induced transparency (MMIT) [1, 33–35]. MMIT, an analog of optomechanically induced transparency [36], which arises from the interference of sidebands generated by the parametric coupling to phonons. This phenomenon further advances the study of magnetically controlled ultraslow light engineering [37, 38]. Moreover, these pioneering works [1, 24, 33, 34] have also brought about a series of novel effects and applications in classical and quantum regimes [39–42]. Notably, high-order sidebands have sparked great interest in optical communications [43], optical and magnonic frequency combs [44, 45] and high-sensitivity measurement [46].

The formation of high-order sidebands is essentially a nonlinear phenomenon, which can be viewed as a parametric process [47]. It is generally recognized that symmetrical optical sideband spectra are generated using frequency combs [48]. As research has advanced, numerous methods for generating frequency combs have been proposed, such as optomechanical frequency combs [49] and optomagnonic frequency combs [50]. Furthermore, frequency combs have been theoretically proposed and experimentally realized in spin waves [51, 52]. The study of high-order optical sideband generation thereby becomes

* yangxs@ujs.edu.cn

† chenyp@ujs.edu.cn

an indispensable part in the field of precision measurement [53]. High-order sidebands have been previously studied in Kerr resonators [54], hybrid optomechanical systems [47, 55], non-Hermitian systems [56], and atom-cavity coupling system [57]. Additionally, it has been proposed that hybrid cavity magnonic systems can generate magnon-induced high-order sidebands [58, 59], which offers a novel approach for producing frequency combs in magnon spintronics [50, 51], and can be utilized for precise detection of nonlinear energy spectra [60] as well as magnon-based precision measurement [61].

Nevertheless, in practice, high-order MMIT sidebands are much weaker than the probe signal, providing substantial hurdles in identifying and employing the second-order sideband [62, 63]. Furthermore, in recent years, there has been tremendous success in researching fast-slow light conversion employing the cavity-magnon system [64, 65]. This progress is achieved by regulating the group delay of the output light field, which is affected via rapid phase dispersion [66, 67]. The slow/fast light effects in the hybrid cavity-magnon system have a wide range of applications in optical communications and interferometry [68, 69].

These aforementioned studies motivate us to look for approaches for improving and controlling the second-order MMIT sidebands and slow/fast light in a CMM system. Despite having similarities to cavity optomechanics [36] and CMM in numerous ways, the direct analysis of second-order sideband generation (SSG) and slow/fast light using a perturbation approach in the optical domain [47], as well as the influence of YIG and a silica microsphere [5], have not been well studied.

In this research, harnessing the MMIT effect, we systematically examine signal transmission, enhanced SSG, and the dynamics of slow/fast light in a hybrid system that combines opto- and magnomechanics. A YIG sphere and a silica sphere are coherently linked through direct physical contact and placed inside a microwave cavity. The YIG sphere contains two modes: a magnon mode and a mechanical vibration mode, which interact via magnetostrictive forces [2]. The silica sphere facilitates an optical whispering-gallery mode (WGM) and a mechanical vibration mode that link together via the optomechanical interaction [36]. The two mechanical modes are coupled via direct physical contact of the two spheres [5]. The magnon mode is further coupled to a microwave cavity mode through magnetic dipole interaction. A strong pump and a weak probe laser field drive the optical cavity (WGM) via the optical fiber, activating the optomechanical anti-Stokes scattering. We derive an analytical solution for the optical transmission rate and SSG efficiency by solving the Heisenberg-Langevin equations through a perturbative approach. Based on our analytical calculations, we show that the transmission rate and SSG exhibits a strong dependence on the magnomechanical, optomechanical, and mechanics mechanics coupling strength (MMCS) between the two microspheres. It is found that by adjusting the MMCS, the

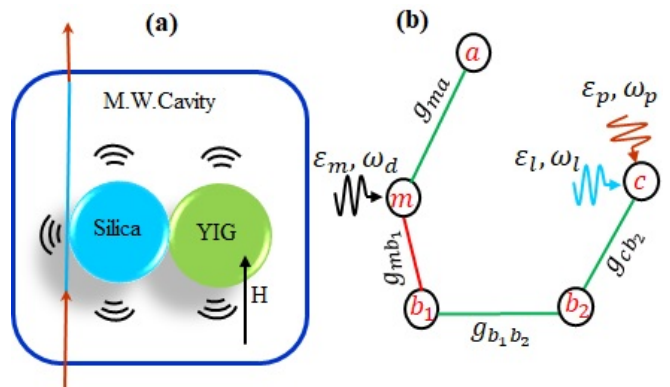


FIG. 1. (a) Sketch of the hybrid system comprising a single-crystal ferromagnetic YIG sphere and a silica sphere that are in physical contact and positioned within a microwave cavity. A strong pump and a weak probe laser field drive the optical cavity (WGM), activating the optomechanical anti-Stokes scattering. The YIG (silica) sphere supports a magnon (an optical) mode and a mechanical mode coupled via the magnetostrictive (optomechanical) interaction. The two localized mechanical modes of the two spheres are directly coupled due to their physical contact. In addition, the magnon mode is powered by a microwave source (not shown) to boost magnomechanical coupling. (b) Diagram of the similar mode-coupling model, exhibiting the interactions between magnons, phonons, and photons.

transmission rate and SSG efficiency can be significantly enhanced, resulting in gains within our system. Furthermore, our study also shows that the efficiency of the SSG can be effectively tuned by adjusting the effective cavity detuning, decay rate, as well as the pump power. Finally, by numerically calculating the group delay, it becomes straightforward to switch between slow and rapid light, which can be further extended by adjusting the relevant parameters. These attributes indicate that our proposed system can serve as a powerful tool for controlling light propagation, with possible applications in optical communication [68], and quantum memories [70].

The structure of this work is as follows: In §II we describe our suggested theoretical model and provide the steady-state solutions for our system. The findings of our research are presented in §III. Finally, in §IV we present a comprehensive conclusion that summarizes the results of our study. In order to ensure the completeness of our work, we give detailed calculations for algebra equations and sideband parameters in §A.

II. Proposed theoretical model

The following section describes the dynamics of our experimentally valid model, as seen in Fig 1. Our setup comprises of a magnomechanical YIG sphere and an optomechanical silica sphere [5], which are coherently connected by direct physical contact and placed inside a microwave cavity. The magnon mode, also known as the Kittel mode [1], is characterized by the collective motion (spin wave) of a significant number of spins in the YIG

sphere. It is triggered by positioning the YIG sphere in a uniform bias magnetic field and applying a microwave drive field, such as through a loop antenna. Because of the large size of the YIG sphere, e.g., a sphere with a diameter of $200\mu\text{m}$ as in Ref [5], a dispersive type interaction is dominant between the magnon mode (at GHz) and the magnetostriction induced mechanical mode (at 10 MHz) [1, 2, 33, 34, 71]. The magnon mode further interacts with a microwave cavity mode through magnetic dipole interaction by positioning the YIG sphere near the maximum magnetic field of the cavity mode [24, 72, 73]. The silica sphere can facilitate both optical WGM and mechanical modes through radiation pressure or photoelastic effect [36]. The intimate contact between the two microspheres causes direct coupling of their mechanical modes. The two spheres are deliberately chosen, such that the mechanical modes are close in frequency and exhibit a linear beamsplitter-type coupling [5]. Therefore, the Hamiltonian for such a hybrid system may be represented as ($\hbar = 1$):

$$\begin{aligned}
H = & \sum_{\substack{j=a,m,c \\ b_1,b_2}} \omega_j j^\dagger j + g_{ma} (m^\dagger a + a^\dagger m) \\
& + g_{mb_1} m^\dagger m (b_1 + b_1^\dagger) - g_{cb_2}^\dagger c^\dagger c (b_2 + b_2^\dagger) \\
& + g_{b_1 b_2} (b_1^\dagger b_2 + b_2^\dagger b_1) + H_{\text{dri}}.
\end{aligned} \quad (1)$$

Here $j = a, m, c, b_1, b_2$ (j^\dagger) are the annihilation (creation) operators of the microwave cavity mode, the magnon mode, the optical cavity mode, and the two mechanical modes, respectively, which satisfy the canonical commutation relation $[j, j^\dagger] = 1$. Where ω_j represents the corresponding resonant frequencies, g_{ma} signifies the cavity-magnon coupling strength, $g_{b_1 b_2}$ is the MMCS between the two microspheres, and g_{mb_1} (g_{cb_2}) is the bare magnomechanical (optomechanical) coupling strength, which may be substantially improved by controlling the magnon mode (optical cavity) with a powerful microwave (laser) field. The driving Hamiltonian $H_{\text{dri}}/\hbar = i\varepsilon_m(m^\dagger e^{-i\omega_d t} - \text{H.c.}) + i\sqrt{\eta_c\gamma_c\varepsilon_l}(c^\dagger e^{-i\omega_l t} - \text{H.c.}) + i\sqrt{\eta_c\gamma_c\varepsilon_p}(c^\dagger e^{-i\omega_p t} - \text{H.c.})$, pertains to the microwave (laser) fields that drive the magnon (optical cavity) modes. The term $\varepsilon_m = \sqrt{5N}/4\gamma H_d$ indicates the coupling strength associated with the magnon mode and the driving magnetic field, in which $N = \rho V$ is the total number of spins (with V shows the volume, and $\rho = 4.22 \times 10^{27}\text{cm}^{-3}$ is the spin density of YIG sphere) [71, 74], $\gamma/2\pi = 28\text{ GHz/T}$ represents the gyromagnetic ratio, with H_d shows the field amplitude. The term $i\sqrt{\eta_c\gamma_c\varepsilon_l}(c^\dagger e^{-i\omega_l t} - \text{H.c.}) + i\sqrt{\eta_c\gamma_c\varepsilon_p}(c^\dagger e^{-i\omega_p t} - \text{H.c.})$ shows the interaction between the WGM and the driving laser through a fiber, which γ_c is the entire loss rate of the cavity fields, which includes the intrinsic loss rate γ_0 and the wave guide coupling rate γ_{ex} ($\gamma_c = \gamma_0 + \gamma_{ex}$) [75, 76]. The coupling parameter $\eta_c = \gamma_{ex}/\gamma_c$ can be frequently adjusted, and we

choose $\eta_c = 0.5$ throughout our study [77]. The symbol $\varepsilon_l = \sqrt{P_l/\hbar\omega_l}$ ($\varepsilon_p = \sqrt{P_p/\hbar\omega_p}$) represent the amplitude of the strong pump (weak probe) field, whereas P_l and P_p are the powers of the corresponding pump and probe fields, respectively.

Similar to previous studies [78, 79], this work primarily focuses on the average response of the entire system to the probing field without considering quantum fluctuation [47]. To investigate the nonlinear dynamics of the system, we use the Heisenberg-Langevin equations and reduce operators to their expected values [i.e., $o(t) = \langle \hat{o} \rangle$ ($o = m, c, a, b_1, b_2$)]. So the Hamiltonian in Eq. (1) leads to the following quantum Langevin equations (QLEs) with respect to $\hbar\omega_d (a^\dagger a + m^\dagger m) + \hbar\omega_l c^\dagger c$, can be expressed as:

$$\begin{aligned}
\langle \dot{m} \rangle = & - (i\Delta_m + \gamma_m) \langle m \rangle - ig_{mb_1} (\langle b_1 \rangle + \langle b_1^\dagger \rangle) \langle m \rangle \\
& - ig_{ma} \langle a \rangle + \varepsilon_m, \\
\langle \dot{c} \rangle = & - (i\Delta_c + \gamma_c) \langle c \rangle + ig_{cb_2} (\langle b_2 \rangle + \langle b_2^\dagger \rangle) \langle c \rangle \\
& + \sqrt{\eta_c\gamma_c}\varepsilon_l + \sqrt{\eta_c\gamma_c}\varepsilon_p e^{-i\delta t}, \\
\langle \dot{a} \rangle = & - (i\Delta_a + \gamma_a) \langle a \rangle - ig_{ma} \langle m \rangle, \\
\langle \dot{b}_1 \rangle = & - (i\omega_{b_1} + \gamma_{b_1}) \langle b_1 \rangle - ig_{mb_1} \langle m^\dagger \rangle \langle m \rangle \\
& - ig_{b_1 b_2} \langle b_2 \rangle, \\
\langle \dot{b}_2 \rangle = & - (i\omega_{b_2} + \gamma_{b_2}) \langle b_2 \rangle + ig_{cb_2} \langle c^\dagger \rangle \langle c \rangle - ig_{b_1 b_2} \langle b_1 \rangle,
\end{aligned} \quad (2)$$

where $\Delta_{a(m)} := \omega_{a(m)} - \omega_d$, $\Delta_c := \omega_c - \omega_l$, $\delta := \omega_p - \omega_l$ are the detunings and γ_j ($j = a, c, m, b_1, b_2$) is the dissipation rate of the corresponding mode.

In the particular situation of $\varepsilon_p \ll \varepsilon_l, \varepsilon_m$, which adheres to the perturbative regime [47, 78], we represent the dynamical parameters as a combination of their steady-state values and small fluctuations, i.e., $o = o_s + \delta o$ ($o = m, m^\dagger, c, c^\dagger, a, a^\dagger, b_1, b_1^\dagger, b_2, b_2^\dagger$), where the first term indicates the steady-state values and the second term shows the small fluctuating terms. Using the perturbation expansion approach in Eq. (2) the steady-state averages of the magnon and optical modes are:

$$\langle m_s \rangle = \frac{\varepsilon_m}{(i\tilde{\Delta}_m + \gamma_m) + \frac{g_{ma}^2}{i\tilde{\Delta}_a + \gamma_a}}, \quad \langle c_s \rangle = \frac{\varepsilon_l}{(i\tilde{\Delta}_c + \gamma_c)}, \quad (3)$$

with the effective detunings $\tilde{\Delta}_m = \Delta_m + 2g_{mb_1}\text{Re}\langle b_{1s} \rangle$ and $\tilde{\Delta}_c = \Delta_c + 2g_{cb_2}\text{Re}\langle b_{2s} \rangle$, which include the frequency shift due to the mechanical displacement jointly caused by the photo- and magnetoelastic interactions. Here we assume that the detunings i.e., $|\Delta_a|, \tilde{\Delta}_m, \tilde{\Delta}_c \simeq \omega_{b_1} \simeq \omega_{b_2} \gg \gamma_j$ ($j = a, c, m, b_1, b_2$), which leads to the following approximate expressions: $\langle m_s \rangle \simeq -i\varepsilon_m/(\tilde{\Delta}_m - g_{ma}^2/\Delta_a)$ and $\langle c_s \rangle \simeq i\varepsilon_l/\tilde{\Delta}_c$. The steady-state averages of the me-

chanical modes are

$$\begin{aligned}\langle b_{1s} \rangle &= \frac{|\langle c_s \rangle|^2 g_{cb_2} g_{b_1 b_2} - |\langle m_s \rangle|^2 g_{mb_1} (i\gamma_{b_2} - \omega_{b_2})}{g_{b_1 b_2}^2 - (i\gamma_{b_1} - \omega_{b_1})(i\gamma_{b_2} - \omega_{b_2})} \\ \langle b_{2s} \rangle &= \frac{|\langle c_s \rangle|^2 g_{cb_2} (i\gamma_{b_1} - \omega_{b_1}) - |\langle m_s \rangle|^2 g_{mb_1} g_{b_1 b_2}}{g_{b_1 b_2}^2 - (i\gamma_{b_1} - \omega_{b_1})(i\gamma_{b_2} - \omega_{b_2})}.\end{aligned}\quad (4)$$

The perturbation terms of Eq. (2) could be formed as follows:

$$\begin{aligned}\dot{\delta m} &= -\left(i\tilde{\Delta}_m + \gamma_m\right) \delta m + G_{mb_1} \left(\delta b_1 + \delta b_1^\dagger\right) \\ &\quad - g_{mb_1} \left(\delta b_1 + \delta b_1^\dagger\right) \delta m - ig_{ma} \delta a, \\ \dot{\delta c} &= -\left(i\tilde{\Delta}_c + \gamma_c\right) \delta c + G_{cb_2} \left(\delta b_2 + \delta b_2^\dagger\right) \\ &\quad + ig_{cb_2} \left(\delta b_2 + \delta b_2^\dagger\right) \delta c + \varepsilon_p e^{-i\delta t}, \\ \dot{\delta a} &= -\left(i\tilde{\Delta}_a + \gamma_a\right) \delta a - ig_{ma} \delta m, \\ \dot{\delta b}_1 &= -\left(i\omega_{b_1} + \gamma_{b_1}\right) \delta b_1 + G_{mb_1} \left(\delta m^\dagger - \delta m\right) \\ &\quad - ig_{b_1 b_2} \delta b_2 - ig_{mb_1} \delta m^\dagger \delta m, \\ \dot{\delta b}_2 &= -\left(i\omega_{b_2} + \gamma_{b_2}\right) \delta b_2 + G_{cb_2} \left(\delta c^\dagger - \delta c\right) \\ &\quad - ig_{cb_2} \delta c^\dagger \delta c - ig_{b_1 b_2} \delta b_1.\end{aligned}\quad (5)$$

Here, $G_{mb_1} = -ig_{mb_1} \langle m_s \rangle$ and $G_{cb_2} = -ig_{cb_2} \langle c_s \rangle$ shows the effective magnon- and optomechanical couplings. The nonlinear terms $g_{mb_1} \delta m (\delta b_1 + \delta b_1^\dagger)$, $g_{cb_2} \delta c (\delta b_2 + \delta b_2^\dagger)$, $ig_{mb_1} \delta m^\dagger \delta m$ and $ig_{cb_2} \delta c^\dagger \delta c$ are taken into consideration to generate the required second-order sidebands, whereas the higher-order sideband terms may be safely omitted owing to their small fluctuations.

To determine the amplitudes of the first (second) order sidebands, we assume that the fluctuation terms in Eq. (5) have the following forms [47, 63]:

$$\begin{aligned}\delta m &= M_{1+} e^{-i\delta t} + M_{1-} e^{i\delta t} + M_{2+} e^{-2i\delta t} + M_{2-} e^{2i\delta t}, \\ \delta c &= C_{1+} e^{-i\delta t} + C_{1-} e^{i\delta t} + C_{2+} e^{-2i\delta t} + C_{2-} e^{2i\delta t}, \\ \delta a_1 &= A_{1+} e^{-i\delta t} + A_{1-} e^{i\delta t} + A_{2+} e^{-2i\delta t} + A_{2-} e^{2i\delta t}, \\ \delta b_1 &= B_{1+} e^{-i\delta t} + B_{1-} e^{i\delta t} + B_{2+} e^{-2i\delta t} + B_{2-} e^{2i\delta t}, \\ \delta b_2 &= X_{1+} e^{-i\delta t} + X_{1-} e^{i\delta t} + X_{2+} e^{-2i\delta t} + X_{2-} e^{2i\delta t}.\end{aligned}\quad (6)$$

The coefficients $C_{y+} (C_{y-})$ represent y th-order ($y = 1, 2, 3, \dots$) lower (upper) sidebands, respectively. By substituting Eq. (6) into Eq. (5) and equating the coefficients of the identical order, one may compute the amplitudes of the first (second) order sidebands (the entire computations and specific constants are included in §A) as [47, 63].

By computing Eqs. (A1) and (A2) we calculate the coefficients for the first and second-order lower sidebands, revealing both the linear and nonlinear features of our system. As a result, the coefficient for the first-order lower sideband is:

$$C_{1+} = \frac{\sqrt{\eta_c \gamma_c} \varepsilon_p}{\alpha_{11}}, \quad (7)$$

and for the second-order lower sideband is:

$$C_{2+} = \frac{\Gamma_1}{\Psi_{17}}. \quad (8)$$

Considering these on hand, by employing the standard input-output relationship, i.e., $s_{\text{out}} = s_{\text{in}} - \sqrt{\eta_c \gamma_c} c(t)$ [80], we get the output fields of our entire system as follows [47, 81]:

$$\begin{aligned}s_{\text{out}} &= s_0 e^{-i\omega_l t} + s_1 e^{-i\omega_p t} - \sqrt{\eta_c \gamma_c} C_{2-} e^{-i(2\omega_p - \omega_l)t} \\ &\quad - \sqrt{\eta_c \gamma_c} C_{1+} e^{-i(2\omega_l - \omega_p)t} - \sqrt{\eta_c \gamma_c} C_{2+} e^{-i(3\omega_l - 2\omega_p)t},\end{aligned}\quad (9)$$

where $s_0 = \varepsilon_l / \sqrt{\eta_c \gamma_c} - \sqrt{\eta_c \gamma_c} c_s$ and $s_1 = \varepsilon_p / \sqrt{\eta_c \gamma_c} - \sqrt{\eta_c \gamma_c} C_{1-}$. The terms $s_0 e^{-i\omega_l t}$ denote the output with pump frequency ω_l , while the terms $s_1 e^{-i\omega_p t}$ and $-\sqrt{\eta_c \gamma_c} C_{1+} e^{-i(2\omega_l - \omega_p)t}$ denote the output signals corresponding to the Stokes and anti-Stokes fields, respectively. Moreover, the terms $-\sqrt{\eta_c \gamma_c} C_{2-} e^{-i(2\omega_p - \omega_l)t}$ and $-\sqrt{\eta_c \gamma_c} C_{2+} e^{-i(3\omega_l - 2\omega_p)t}$ describe the output fields at the frequencies $\omega_l + 2\Omega$ ($\omega_l - 2\Omega$), corresponding to the upper (lower) SSG.

The optical transmission rate of the probe field may be calculated as:

$$T = |t_p|^2 = \left| 1 - \frac{\sqrt{\eta_c \gamma_c} C_{1+}}{\varepsilon_p} \right|^2. \quad (10)$$

It is crucial to note that our emphasis here is on the lower SSG process. To do this, we establish the dimensionless quantity:

$$\eta_s = \left| -\frac{\sqrt{\eta_c \gamma_c} C_{2+}}{\varepsilon_p} \right|, \quad (11)$$

which demonstrates the efficiency of the lower SSG.

III. Results

In the preceding section, we determined the transmission rate and SSG efficiency of the output probe field for our coupled opto- and magnomechanical microsphere system. In this section, we present our numerical findings for investigating the transmission rate, SSG efficiency, and group delays of our system using a set of experimentally feasible parameter values [2, 5]: $\omega_{a,m}/2\pi = 7.86$ GHz, $\omega_{b_1}/2\pi = 20.15$ MHz, $\omega_{b_2}/2\pi = 20.11$ MHz. We take the microwave (optical) cavity decay rate and magnon decay rates $\gamma_{a(c),m}/2\pi = 1$ MHz, which are the typical values in the cavity magnonic experiments [24, 73], optical cavity resonance wavelength $\lambda = 1550$ nm, $\gamma_{b_1, b_2}/2\pi = 1$ KHz, $g_{ma}/2\pi = 1$ MHz, $g_{b_1, b_2}/2\pi = 1$ MHz, $g_{mb_1}/2\pi = 0.1$ Hz [2] and the drive magnetic field $H_d = 3.5$ mT. The parameters for the YIG sphere are as follows: diameter $D = 200 \mu\text{m}$ [5], the spin density $\rho = 4.22 \times 10^{27} \text{cm}^{-3}$. In addition, we take the power

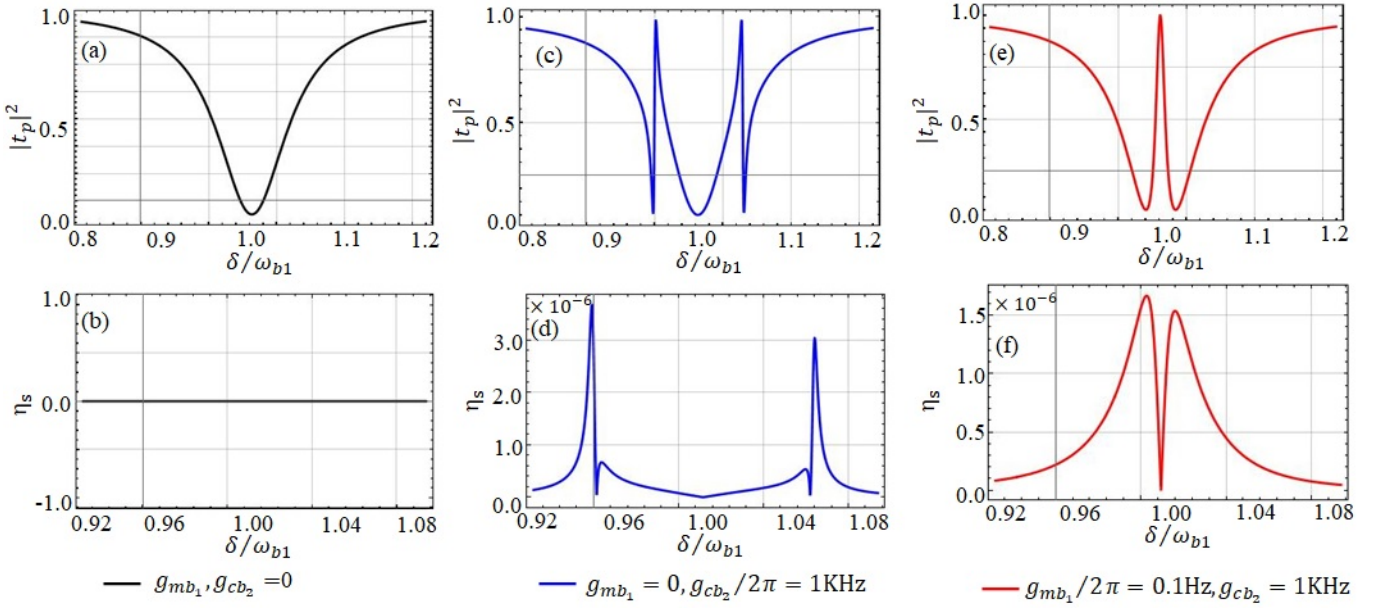


FIG. 2. Simulation results of the transmission rate of the probe field $|t_p|^2$ and efficiency (η_s) of SSG versus optical detuning δ/ω_{b1} . We choose for (a) and (b) $g_{mb1} = 0$ and $g_{cb2} = 0$, (c) and (d) $g_{mb1} = 0$ and $g_{cb2}/2\pi = 1$ KHz, and (e) and (f) $g_{mb1}/2\pi = 0.1$ Hz and $g_{cb2}/2\pi = 1$ KHz. The other parameter values are considered as: $\omega_{a,m}/2\pi = 7.86$ GHz, $\omega_{b1}/2\pi = 20.15$ MHz, $\omega_{b2}/2\pi = 20.11$ MHz, $\gamma_{a(c),m}/2\pi = 1$ MHz, $\lambda = 1550$ nm, $\gamma_{b1b2}/2\pi = 1$ KHz, $g_{ma}/2\pi = 1$ MHz, $g_{b1b2}/2\pi = 1$ MHz, $H_d = 3.5$ mT, $D = 200\mu\text{m}$, $\rho = 4.22 \times 10^{27} \text{cm}^{-3}$, $\hbar = 1.054 \times 10^{-34} \text{J} \cdot \text{s}$, $N = 3 \times 10^{16}$, $\gamma = 2\pi \times 28$ GHz/T, $P_l = 10$ mW, $\varepsilon_p = 0.01\varepsilon_l$, $\Delta_a = \hat{\Delta}_m = -\omega_{b1}$ and $\hat{\Delta}_c = \omega_{b2}$.

of the pump field $P_l = 10$ mW, and the amplitude of the probe field $\varepsilon_p = 0.01\varepsilon_l$, with $\Delta_a = \hat{\Delta}_m = -\omega_{b1}$ and $\hat{\Delta}_c = -\omega_{b2}$. Unless stated otherwise, we use the aforementioned variables throughout this section.

In §III A, we examine the impact of magnomechanical, optomechanical, and MMCS on the transmission rate and the SSG efficiency spectrum of the output probe field. We extend the investigation to produce magnomechanically induced absorption (MMIA) and MMIT with the assistance of magnomechanical and optomechanical coupling strengths. Next, in §III B, we study the dependence of SSG on the effective cavity detuning $\hat{\Delta}_c$ and decay rate γ_c . Further, in §III C, we investigate the effects of pump power on the efficiency of SSG. Finally, in §III D, we explore the control of slow/fast light in our system.

A. Effect of magnomechanical, optomechanical, and MMCS on transmission rate and SSG efficiency

In the subsequent subsection, we are interested in investigating the influence of opto-magnomechanical and MMCS on the transmission rate ($|t_p|^2$) and the SSG efficiency (η_s) of the output probe field.

We start our investigation by considering the effect of opto-magnomechanical coupling strengths on the transmission rate and the SSG efficiency. Figure 2 displays the transmission rate ($|t_p|^2$) and the SSG efficiency (η_s) of the output probe field versus optical detuning (δ/ω_{b1}) for different sets of opto-magnomechanical coupling strengths. In Fig. 2(a-b), we assume that both

the opto-magnomechanical coupling strengths are absent ($g_{mb1} = 0$ and $g_{cb2} = 0$). Under these considerations, Fig. 2(a) shows a typical Lorentzian shape in the transmission spectra, with a minimum at the resonance point ($\delta = \omega_{b1}$). This indicates that our system exhibits MMIA at $\delta = \omega_{b1}$. Likewise, the SSG efficiency η_s spectrum, illustrated in Fig. 2(b), reveals a value of zero. This occurs because the nonlinear terms in Eq.(5)—specifically $g_{mb1}\delta m(\delta b_1 + \delta b_1^\dagger)$, $g_{cb2}\delta c(\delta b_2 + \delta b_2^\dagger)$, $ig_{mb1}\delta m^\dagger\delta m$, and $ig_{cb2}\delta c^\dagger\delta c$ —responsible for SSG, are all zero. Consequently, the SSG efficiency η_s is also zero. As shown in Figs. 2(c-d), when the opto-magnomechanical coupling strengths are set to $g_{mb1} = 0$ and $g_{cb2}/2\pi = 1$ KHz, we observe a central absorption dip at the resonance point ($\delta = \omega_{b1}$). Additionally, two Fano-like resonance peaks frequently appear on both sides of the absorption window in the probe field transmission spectrum [see Fig. 2(c)]. Meanwhile, the SSG spectrum also shows two asymmetric Fano peaks located at $\delta \simeq 0.96\omega_{b1}$ and $\delta \simeq 1.06\omega_{b1}$ [see Fig. 2(d)]. Physically, the basic origin for the emergence of these Fano-like peaks is the presence of non-resonant interactions. For instance, in a conventional optomechanical system, if the anti-Stokes process is not resonant with the cavity frequency, the spectrum will exhibit asymmetric Fano-like profiles [82, 83]. The maximum value of the SSG efficiency is about 3.4×10^{-6} , as shown by the solid blue curve in Fig. 2(d). In general, the SSG efficiency in the CMM system is fairly low, which is governed by the cou-

pling rate and the pump power of the CMM system. The emergence of SSG is primarily due to the up-conversion of the first-order sideband. In the preceding scenario $\delta = \omega_{b_1}$, the anti-Stokes field experiences a resonant enhancement, resulting in the suppression of SSG [54].

Similarly, in Figs. 2(e-f), when both opto-magnomechanical coupling strengths are nonzero, one may find from Fig. 2(e) that the curve of $|t_p|^2$ exhibits a conventional MMIT profile. This profile features a transmission peak at $\delta = \omega_{b_1}$, with a linewidth of approximately 3 MHz, flanked by two deep absorption valleys at $\delta \approx 0.985\omega_{b_1}$ and $\delta \approx 1.015\omega_{b_1}$. This phenomenon can be explained by destructive interference between the probe field and the anti-Stokes field, which results in the creation of a transparency window at $\delta = \omega_{b_1}$. Correspondingly, the SSG spectrum η_s shown in Fig. 2(f) exhibits two peaks and a local minimum at the resonance condition $\delta = \omega_{b_1}$.

Let us investigate how the MMCS ($g_{b_1 b_2}$) between the two microspheres affects the optical transmission rate $|t_p|^2$ and the SSG efficiency η_s spectrum. To do this, we plotted the transmission rate ($|t_p|^2$) and the SSG efficiency (η_s) of the output probe field against optical detuning (δ/ω_{b_1}) for different values of the MMCS ($g_{b_1 b_2}$), as shown in Fig. 3(a-b). In Fig. 3(a), for a MMCS of $g_{b_1 b_2}/2\pi = 1$ MHz, the system exhibits a transmission window at the resonance frequency ($\delta = \omega_{b_1}$), with two absorption peaks appearing symmetrically on either side of the resonance, as depicted by the black solid curve in the Fig. 3(a). As anticipated, adjusting the MMCS to $g_{b_1 b_2}/2\pi = 3$ MHz results in a higher peak amplitude of the transparency window. Additionally, the right absorption dip becomes more pronounced, while the left absorption peak narrows. Interestingly, when the MMCS is set to $g_{b_1 b_2}/2\pi = 6$ MHz, we observe that the transparency window not only narrows and shifts away from the resonance point, but its amplitude also increases significantly, indicating amplification in our system, as indicated by the red-colored solid line in Fig. 3(a).

Further, the dependence of SSG efficiency η_s on the MMCS ($g_{b_1 b_2}$) is illustrated in Fig. 3(b). It is obvious that when $g_{b_1 b_2}/2\pi = 1$ MHz the SSG efficiency spectrum generates two peaks, with the dip at the resonance point [refer to the black solid curve in 3(b)]. When setting $g_{b_1 b_2}/2\pi = 3$ MHz, the right peak in the efficiency spectrum decreases, while the left peak is enhanced and the dip shifts away from the resonance point. Notably, when we set $g_{b_1 b_2}/2\pi = 6$ MHz, the SSG efficiency spectrum mimics a line with an asymmetric peak. The right peak is more compressed and almost vanishes on the right side of the resonance point. In contrast, the left peak becomes sharper, with a peak value of $\approx 8.9 \times 10^{-6}$ locating at $\delta \approx 0.95\omega_{b_1}$ [see the red solid curve in 3(b)]. The asymmetry of the SSG spectrum is caused by constructive and destructive interference between the direct SSG process and the up-converted first-order sideband process [84]. To provide direct insight into the influence of $g_{b_1 b_2}$ on the efficiency of the SSG, Fig. 3(c) presents the

contour map of the efficiency η_s (in logarithmic form) of the SSG as a function of both the MMCS and the detuning (δ/ω_{b_1}). This figure illustrates that the efficiency of the SSG undergoes significant changes with the increase of MMCS. The maximum SSG efficiency is found in the bright red region, as indicated by the black dotted arrow [see Fig. 3(c)].

In the above discussion, we note that increasing the MMCS ($g_{b_1 b_2}$) in our coupled opto- and magnomechanical microspheres system enhances the transmission rate and the SSG efficiency due to improved energy transfer and interaction dynamics. Stronger MMCS facilitates more efficient coupling between the mechanical modes, leading to enhanced coherence and energy exchange. This results in a more pronounced interaction between the optical and magnomechanical components, boosting the overall transmission rate and increasing the efficiency of SSG.

B. Dependence of the SSG efficiency on the detuning $\tilde{\Delta}_c$ and decay rate γ_c

The effective cavity detuning ($\tilde{\Delta}_c$) and the decay rate (γ_c) also significantly impact the SSG efficiency. In the following, we demonstrate how the SSG efficiency changes with different detuning and decay rates.

In Fig. 4(a), we plotted the SSG efficiency versus the scaled detuning (δ/ω_{b_1}) for various effective cavity detuning settings ($\tilde{\Delta}_c$). As shown in Fig. 4(a), by adjusting the detuning, the SSG efficiency can be significantly modified, leading to an overall improvement in the SSG efficiency. When we set $\tilde{\Delta}_c/2\pi = 20.11$ MHz, we observe two symmetric peaks on either side of the resonance point ($\delta = \omega_{b_1}$), with a peak value of approximately 1.65×10^{-6} [see the blue dotted line in Fig. 4(a)]. Increasing the detuning to $\tilde{\Delta}_c/2\pi = 21.11$ MHz significantly enhances the efficiency peak on the left side of the resonance point, while the peak on the right side is substantially suppressed [see black dashed line in Fig. 4(a)]. Further increasing the detuning to $\tilde{\Delta}_c/2\pi = 22.11$ MHz transforms the initially symmetric peaks into an enhanced asymmetric efficiency peak with a much narrower bandwidth and a peak value of approximately 7.6×10^{-6} [see the red solid line in Fig. 4(a)]. The physical reason behind this phenomenon is that as the detuning increases, the system moves away from exact resonance, leading to an asymmetric distribution of energy. This asymmetry causes an enhancement of the SSG efficiency on one side of the resonance point while suppressing it on the other. Thus, by adjusting the effective detuning, one can control both the SSG efficiency and the symmetry of the generated peaks. This capability is essential for optimizing the performance of opto-magnomechanical devices and may provide a tool to achieve high-precision measurement [20–22].

In the following, we examine the impact of the decay rate (γ_c) on the efficiency of SSG. In Fig. 4(b), the efficiency (η_s) of SSG is depicted as a function of the detuning (δ/ω_{b_1}) for different decay rates (γ_c). This figure

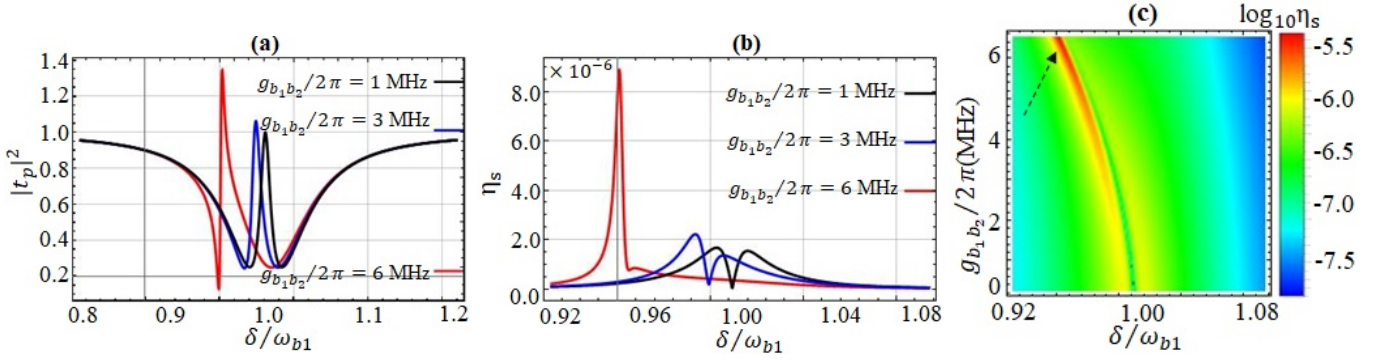


FIG. 3. (a-b) Transmission rate of the probe field $|t_p|^2$ and efficiency (η_s) of SSG versus optical detuning δ/ω_{b_1} is shown for different values of MMCS between the two microspheres: $g_{b_1b_2}/2\pi = 1$ MHz, $g_{b_1b_2}/2\pi = 3$ MHz and $g_{b_1b_2}/2\pi = 6$ MHz. (c) Contour map of SSG efficiency η_s (in logarithmic form) vs optical detuning δ/ω_{b_1} and MMCS $g_{b_1b_2}$. All the remaining variables are similar as in Fig. 2(f).

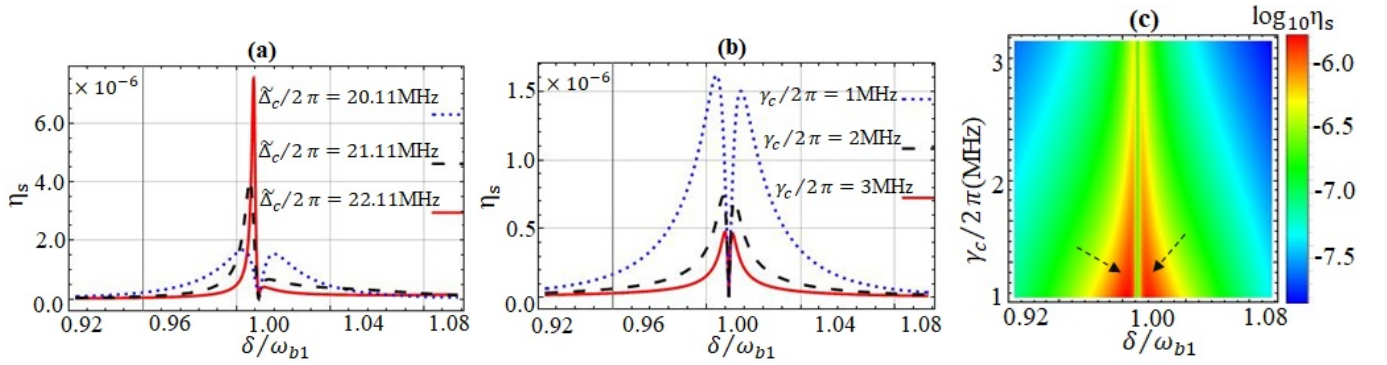


FIG. 4. The calculated result of SSG efficiency (η_s) as a function of optical detuning (δ/ω_{b_1}). (a) For various values of effective detuning: $\tilde{\Delta}_c/2\pi = 20.11$ MHz (blue dotted curve), $\tilde{\Delta}_c/2\pi = 21.11$ MHz (black dashed curve), and $\tilde{\Delta}_c/2\pi = 22.11$ MHz (red solid curve). (b) For various values of decay rate: $\gamma_c/2\pi = 1$ MHz (blue dotted curve), $\gamma_c/2\pi = 2$ MHz (black dashed curve), and $\gamma_c/2\pi = 3$ MHz (red solid curve). (c) Contour map of SSG efficiency η_s (in logarithmic form) vs optical detuning δ/ω_{b_1} and decay rate ($\gamma_c/2\pi$ (MHz)). All the remaining variables are similar as in Fig. 2(f).

demonstrates that as the decay rate increases $\gamma_c/2\pi = 1$ MHz to $\gamma_c/2\pi = 3$ MHz, the SSG process diminishes not only around both sides of the resonance point ($\delta = \omega_{b_1}$), but also drastically reduces the linewidth of the SSG. This phenomenon can be explained as follows: Increasing the decay rate (γ_c) of the WGM mode reduces the SSG efficiency in a coupled opto- and magnomechanical microsphere system because a higher decay rate results in increased energy dissipation within the system. This higher dissipation reduces the effective interaction strength between the optical and magnomechanical components, lowering the efficiency of side-band production. As a result, the energy available for creating SSG is decreased, resulting in lesser efficiency [57].

To gain a more comprehensive analysis, the contour map of the calculated SSG efficiency η_s (in logarithmic form) is plotted as a function of the optical detuning δ/ω_{b_1} and the decay rate γ_c , as shown in Fig. 4(c). The figure demonstrates that the efficiency of the SSG decreases significantly as the decay rate (γ_c) increases. The highest value of the SSG efficiency is observed at lower

decay rates, as indicated by the black dotted arrows on either side of the resonance point [see Fig. 4(c)]. As the decay rate increases, the color of the density plot shifts from red to blue, indicating a decrease in the SSG efficiency.

In light of the aforementioned considerations, we can describe the following aspects as influenced by the effective cavity detuning ($\tilde{\Delta}_c$) and decay rate (γ_c) on SSG efficiency (η_s). (i) Increasing the detuning can enhance the SSG efficiency, causing the initially symmetric peaks to merge into an asymmetric peak. Additionally, these peaks can shift and exhibit narrower linewidths based on variations in the detuning. (ii) An increase in the decay rate (γ_c) significantly reduces the formation of the SSG efficiency.

C. Effects of pump power on the efficiency of SSG generation

It is worth noting that the pump power (P_i) is a crucial parameter that will inevitably influence the efficiency (η_s) of SSG [47, 85]. To clearly illustrate the impact of the pump power on efficiency (η_s) of the SSG, we plot

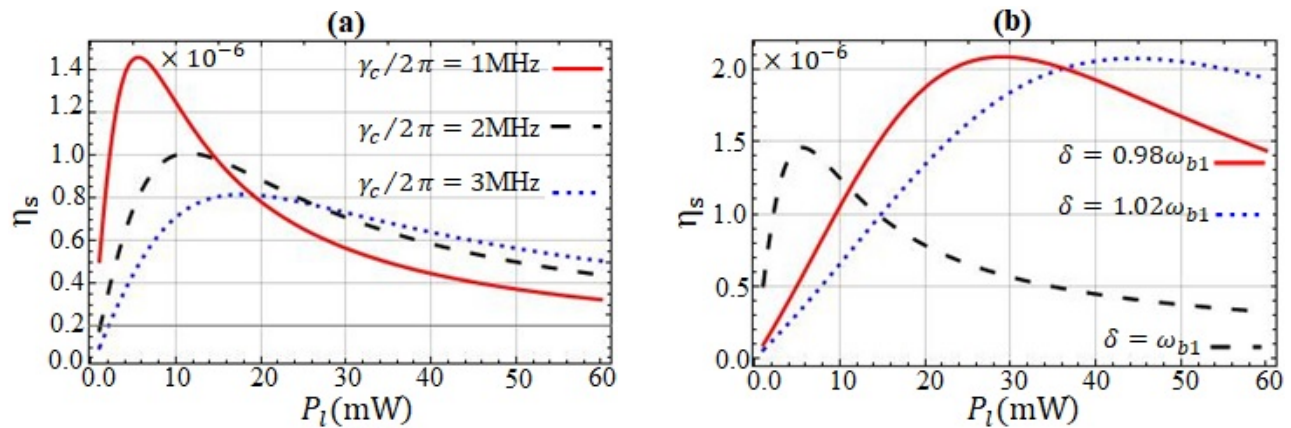


FIG. 5. The analytical results of SSG efficiency (η_s) as a function of pump power $P_l(mW)$: (a) For various values of decay rate: $\gamma_c/2\pi = 1$ MHz (red solid curve), $\gamma_c/2\pi = 2$ MHz (black dashed curve), and $\gamma_c/2\pi = 3$ MHz (blue dotted curve) at $\delta = \omega_{b_1}$. (b) For various values of optical detuning: $\delta = 0.98\omega_{b_1}$ (red solid curve), $\delta = \omega_{b_1}$ (black dashed curve) and $\delta = 1.02\omega_{b_1}$ (blue dotted curve). All the remaining variables are similar as in Fig. 2(f).

the efficiency (η_s) versus the power (P_l) in Fig. 5.

Now, let us investigate the sensitivity of SSG efficiency to variations in the decay rate (γ_c). According to Fig. 5(a), the enhancement of SSG is remarkable as the power is increased up to $P_l = 10(mW)$, with a peak value of approximately 1.42×10^{-6} [see the red solid curve in Fig. 5(a)]. However, with a further increase in pump power, the efficiency η_s sharply decreases and eventually stabilizes. The red solid, black dashed and blue dotted lines correspond to $\gamma_c/2\pi = 1$ MHz, $\gamma_c/2\pi = 2$ MHz, and $\gamma_c/2\pi = 3$ MHz in Fig. 5(a) respectively. It is crucial to notice that the peak efficiency value is obtained at the lowest decay rate, which is consistent with our earlier results in Fig. 4 (b,c). Increasing the decay rate decreases the SSG efficiency.

Correspondingly, in Fig. 5(b) we show a graph of the SSG efficiency η_s versus pump power $P_l(mW)$ for various optical probe field detuning δ values. We choose the values of optical detuning $\delta = 0.98\omega_{b_1}$ (red solid curve), $\delta = \omega_{b_1}$ (black dashed curve), and $\delta = 1.02\omega_{b_1}$ (blue dotted curve) [see Fig. 5(b)]. From Fig. 5(b), it is evident that for all values of probe detuning, an initial small increase in pump power leads to a sharp rise in the SSG efficiency. However, as the pump power continues to increase, the efficiency begins to decrease. It is important to note that the lowest peak efficiency is observed at the resonance point $\delta = \omega_{b_1}$ (black dashed curve), while the highest efficiency values are achieved at $\delta = 0.98\omega_{b_1}$ (red solid curve) and $\delta = 1.02\omega_{b_1}$ (blue dotted curve). This observation aligns with our previous findings that maximum efficiency is attained on either side of the resonance point, whereas at the resonance point itself, the efficiency drops to zero [see Figs. 3-4]. The substantial improvement of SSG along with a much smaller bandwidth is important for prospective applications in weak signal sensing [86, 87], e.g., precise sensing of weak forces [88] and charges [86, 87].

D. Group delay: slow and fast light control

In general, the hybrid cavity opto- and magnomechanical systems not only produce absorption and transmission effects but also enable the manipulation of light propagation, including slow/fast light phenomena [38, 63]. The slow light phenomenon is a crucial application for Fano resonance and EIT systems [89], keeping photons inside the system for an extended period of time, which helps improve the interactions between light and matter. Generally, this feature can be quantitatively characterized by the group delay. The optical group delay of the output probe light may be described as [59, 78]:

$$\tau_1 = \left. \frac{d \arg(t_p)}{d\delta} \right|_{\delta=\omega_{b_1}}, \quad (12)$$

here, $\arg(t_p)$ denotes the transmission phase. The group delay of the second-order sideband may be expressed as:

$$\tau_2 = \left. \frac{d \arg(C_{2+})}{2d\delta} \right|_{\delta=\omega_{b_1}}. \quad (13)$$

A group delay larger than zero ($\tau_1 > 0$) implies slow light, whereas a negative group delay ($\tau_1 < 0$) is associated with rapid light. Recent advances in slow-light investigations have led to developments in a variety of applications, including telecommunications and optical data storage.

A key feature of our framework is its tendency to generate either slow or rapid light by altering the system parameters. In Fig. 6, we plot the group delay $\tau_1(\mu s)$ of the probe light and the group delay $\tau_2(\mu s)$ of SSG as a function of the pump power P_l (mW), for various values of magnomechanical and optomechanical coupling strengths. First, we consider the scenario in which both coupling strengths are zero ($g_{mb_1} = g_{cb_2} = 0$).

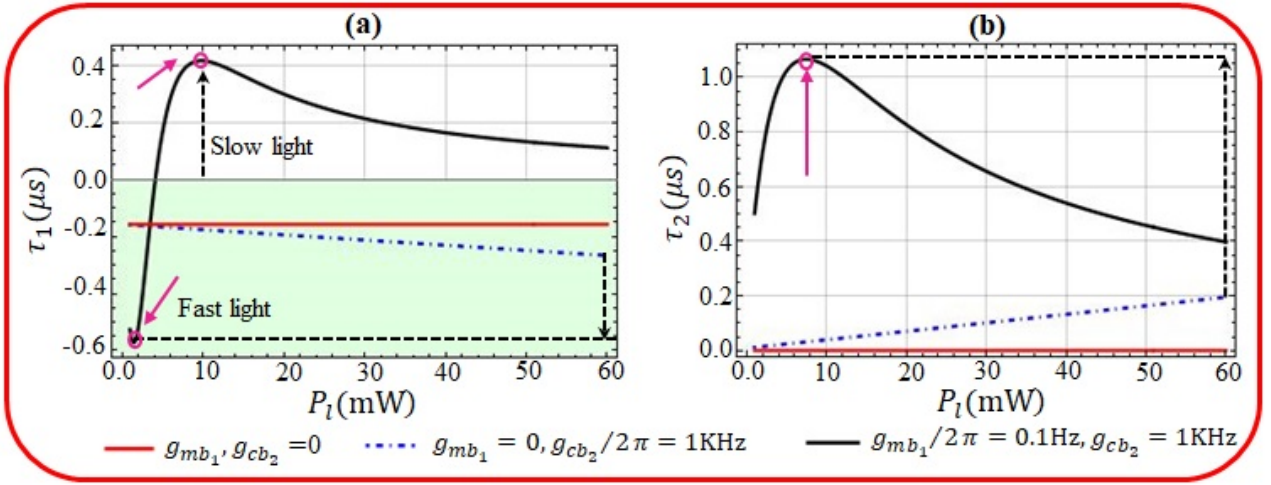


FIG. 6. Simulation results of the optical group delay $\tau_1(\mu\text{s})$ of the probe light and the group delay $\tau_2(\mu\text{s})$ of SSG as a function of the pump power P_l (mW), for various values of magnomechanical and optomechanical coupling strengths. The chosen parameters are: $g_{mb_1} = 0, g_{cb_2} = 0$ (red solid curve), $g_{mb_1} = 0, g_{cb_2}/2\pi = 1$ KHz (blue dotted-dashed curve), and $g_{mb_1}/2\pi = 0.1$ Hz, $g_{cb_2}/2\pi = 1$ KHz (black solid curve). All the remaining variables are similar as in Fig. 2(f), except for $\delta = \omega_{b_1}$.

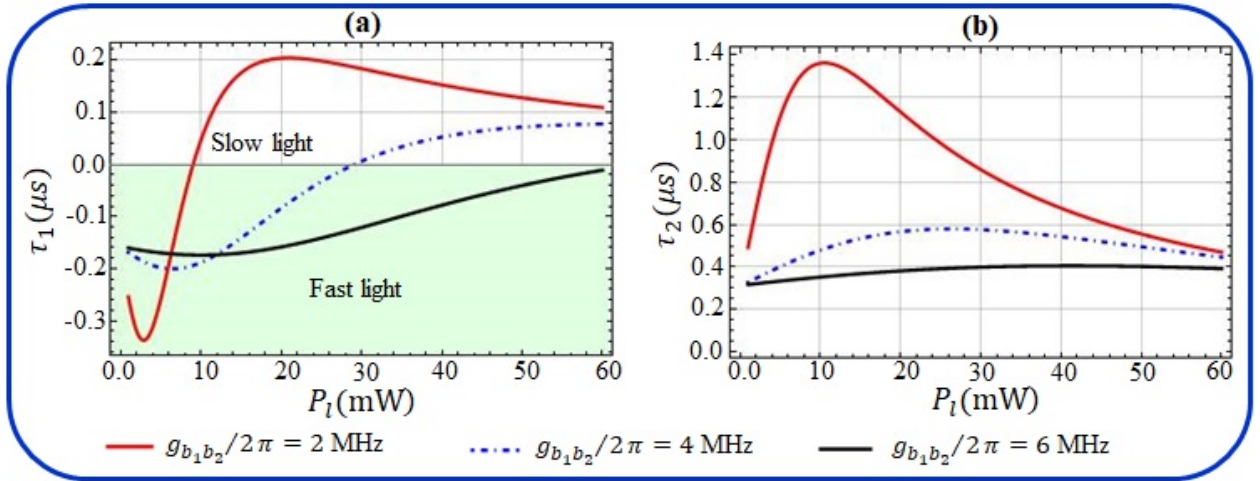


FIG. 7. Simulation results of the group delay $\tau_1(\mu\text{s})$ of the transmitted probe field and the group delay $\tau_2(\mu\text{s})$ of SSG as a function of the pump power P_l (mW), for several values of MMCS between the two microspheres: $g_{b_1b_2}/2\pi = 2$ MHz (red solid curve), $g_{b_1b_2}/2\pi = 3$ MHz (blue dotted-dashed curve), and $g_{b_1b_2}/2\pi = 6$ MHz (black solid curve). All the remaining variables are similar as in Fig. 2(f), except for $\delta = \omega_{b_1}$.

In this case, the first-order group delay τ_1 remains approximately constant at $-0.16\mu\text{s}$, while the second-order group delay τ_2 is zero [see red solid curve in Fig. 6(a,b)]. The physical explanation is that with zero couplings, the nonlinear terms are absent, resulting in a second-order group delay $\tau_2(\mu\text{s})$ of zero. When setting $g_{mb_1} = 0, g_{cb_2}/2\pi = 1$ KHz the first-order group delay increases continuously in the negative direction as pump power increases, indicating a fast light effect. Conversely, the second-order group delay increases steadily in the positive direction with rising pump power, reflecting a slow light effect [see blue dotted-dashed curve in Fig. 6(a,b)]. More interestingly, when both coupling strengths are

present $g_{mb_1}/2\pi = 0.1$ Hz, and $g_{cb_2}/2\pi = 1$ KHz, for small increases in pump power, the first-order group delay τ_1 sharply transitions from negative to positive values (approximately $0.4\mu\text{s}$), then decreases and eventually stabilizes. This behavior suggests that an adjustable switch from rapid to slow light can be achieved [note the black solid line in Fig. 6(a)]. In contrast, although the second-order group delay increases abruptly, it never transitions between negative and positive values, hence the total light is slow light in this situation [note the black solid line in Fig. 6(b)].

We now investigate the impact of MMCS between the two microspheres ($g_{b_1b_2}$) on the first and second order

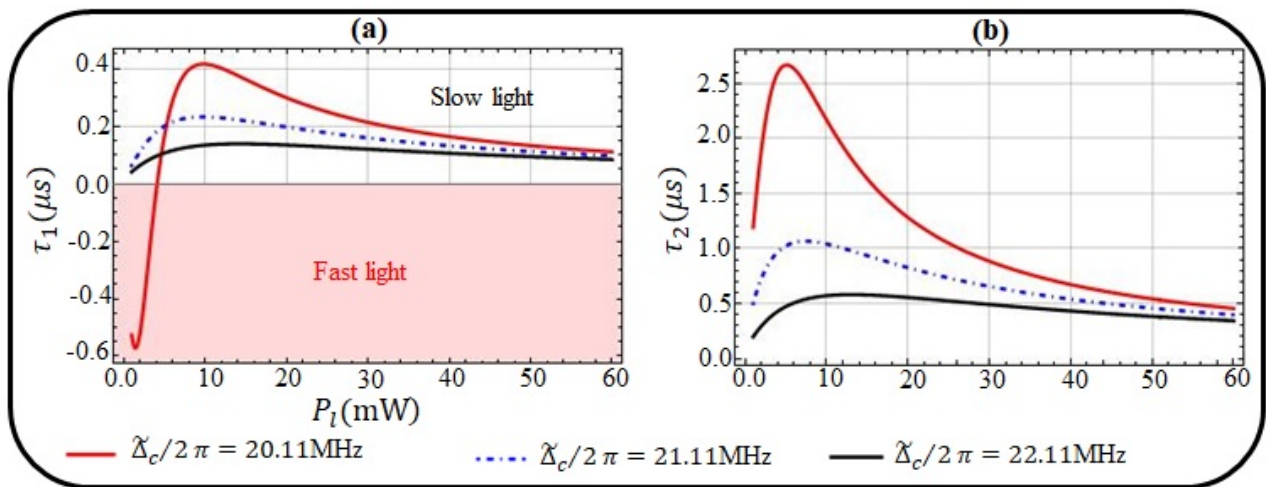


FIG. 8. Analytical results for the group delay $\tau_1(\mu\text{s})$ of the transmitted probe light and the group delay $\tau_2(\mu\text{s})$ of SSG as a function of the pump power P_l (mW), for several values of effective detuning: $\tilde{\Delta}_c/2\pi = 20.11$ MHz (red solid curve), $\tilde{\Delta}_c/2\pi = 21.11$ MHz (blue dotted-dashed curve), and $\tilde{\Delta}_c/2\pi = 22.11$ MHz (black solid curve). All the remaining variables are similar as in Fig. 2(f), except for $\delta = \omega_{b_1}$.

group delays. In Fig. 7 (a,b), we illustrate the plot of first and second order group delays for various values of MMCS. Initially, when we set MMCS $g_{b_1 b_2}/2\pi = 2$ MHz for smaller pump power, both the first and second order group delays grow rapidly and then decrease [see red solid curve in Fig. 7 (a,b)]. However, only the first-order group delay transitions from negative to positive, with slow light being dominant. This indicates that both fast and slow light effects can be achieved [see solid curve in Fig. 7 (a)]. In general, as the MMCS increases to $g_{b_1 b_2}/2\pi = 4$ MHz, the first-order group delay transitions from fast to slow light with the rise in pump power. The peak value of the group delay significantly decreases, and the durations of both slow and fast light regions become nearly equal [see blue dotted-dashed curve in Fig. 7(a)]. Although the second-order group delay also increases with the pump power, its peak value drops from $1.38\mu\text{s}$ to $0.6\mu\text{s}$. However, the fundamental pattern of alternating between rapid and slow light effects remains unchanged [note the blue dotted-dashed curve in Fig. 7(b)]. More interestingly, at $g_{b_1 b_2}/2\pi = 6$ MHz, while the first-order group delay changes with increasing pump power, the overall light remains fast [as seen by the black solid curve in 7(a)]. The fundamental physical reason is that by adding active gain to the system, rapid light may be observed in experiments [90, 91]. This active gain is clearly visible in our previous results [as seen by the red solid curve in Fig. 3(a)]. It is distinctly observable that the performance of the second-order sideband group delay changes slightly at $g_{b_1 b_2}/2\pi = 6$ MHz [see black solid curve in Fig. 7(b)].

Finally, we study how to control group delay via effective detuning $\tilde{\Delta}_c$. In Fig. 8, we display the first and second-order group delays as a function of the pump power P_l and different values of effective detuning. In

Fig. 8(a), when we choose $\tilde{\Delta}_c/2\pi = 20.11$ MHz [see red solid curve in Fig. 8(a)] the group delay experiences the conversion from fast to slow light as the pump power increases. The delay reaches a peak value, then decreases, and eventually stabilizes at a saturated numerical value with further increases in pump power. However, the second-order group delay increases rapidly, then decreases, and ultimately stabilizes as the power increases, without undergoing any transitions [see red solid curve in Fig. 8(b)]. On increasing effective detuning $\tilde{\Delta}_c/2\pi = 21.11$ to $\tilde{\Delta}_c/2\pi = 22.11$ in both the first and second-order group delay cases, although the peak value of the group delay decreases, slow light remains dominant over most of the region [see blue dotted-dashed and black solid curves in Fig. 8(a,b)]. Consequently, with regulating the effective detuning the slow-to-fast light can be easily achieved in our system. These findings suggest that our system can act as a tunable switch that can be adjusted using a variety of system parameters. This capability can be leveraged in optical storage or quantum communication applications [70, 92, 93].

IV. Conclusions

In conclusion, we have presented a practical and efficient scheme to enhance and steer the MMIT, SSG, and group delay employing two coupled opto- and magnomechanical microspheres placed inside a microwave cavity. We obtained analytical formulations for the transmission rate and SSG by solving the Heisenberg-Langevin equations using a perturbation approach. We have shown that the transmission rate and SSG exhibits a strong dependence on the magnomechanical, optomechanical, and MMCS between the two microspheres. It was demonstrated that modulating MMCS can boost the transmission rate and SSG efficiency while simultaneously trans-

forming two symmetrical SSG peaks into an asymmetric Fano-like peak. In particular, we have analyzed the effects of effective cavity detuning, decay rate, and pump power on SSG efficiency. Finally, by examining the group delay of the probe light, we investigated the conditions for slow/fast light propagation in our system, which may be adjusted by modifying various system variables. Beyond its fundamental scientific significance, our research has important practical implications. These findings are applicable to real-world experiments where controlling light transmission is crucial, potentially benefiting applications such as microwave-optical conversion modulation, optical storage, and high-precision measurement.

Acknowledgements

Abdul Wahab is grateful for the financial assistance granted by the China Postdoctoral Research Council and Jiangsu University. This project was funded by the Natural Science Foundation of Jiangsu Province (Grant No. BK20231320), National Natural Science Foundation of China (Grant No. 12174157) and Jiangsu Funding Program for Excellent Postdoctoral Talent No.2024ZB867.

A. Appendix

1. Calculations of first-order sideband

In this appendix, we present detailed calculations to obtain the amplitudes of the first-order sideband:

$$\begin{aligned}
M_{1+}h_1 &= G_{mb_1}(B_{1-}^* + B_{1+}) - ig_{ma}A_{1+}, \\
M_{1-}h_2 &= G_{mb_1}(B_{1+}^* + B_{1-}) - ig_{ma}A_{1-}, \\
C_{1+}h_3 &= G_{cb_2}(X_{1-}^* + X_{1+}) + \varepsilon_p, \\
C_{1-}h_4 &= G_{cb_2}(X_{1+}^* + X_{1-}), \\
A_{1+}h_5 &= -ig_{ma}M_{1+}, \\
A_{1-}h_6 &= -ig_{ma}M_{1-}, \\
B_{1+}h_7 &= G_{mb_1}(M_{1-}^* - M_{1+}) - ig_{b_1b_2}X_{1+}, \\
B_{1-}h_8 &= G_{mb_1}(M_{1+}^* - M_{1-}) - ig_{b_1b_2}X_{1-}, \\
X_{1+}h_9 &= G_{cb_2}(C_{1-}^* - C_{1+}) - ig_{b_1b_2}B_{1+}, \\
X_{1-}h_{10} &= G_{cb_2}(C_{1+}^* - C_{1-}) - ig_{b_1b_2}B_{1-}.
\end{aligned} \tag{A1}$$

with $h_1 = -i\delta + i\tilde{\Delta}_m + \gamma_m$, $h_2 = i\delta + i\tilde{\Delta}_m + \gamma_m$, $h_3 = -i\delta + i\tilde{\Delta}_c + \gamma_c$, $h_4 = i\delta + i\tilde{\Delta}_c + \gamma_c$, $h_5 = -i\delta + i\tilde{\Delta}_a + \gamma_a$, $h_6 = i\delta + i\tilde{\Delta}_a + \gamma_a$, $h_7 = -i\delta + i\omega_{b_1} + \gamma_{b_1}$, $h_8 = i\delta + i\omega_{b_1} + \gamma_{b_1}$, $h_9 = -i\delta + i\omega_{b_2} + \gamma_{b_2}$, and $h_{10} = i\delta + i\omega_{b_2} + \gamma_{b_2}$.

After solving Eq. (A1) for (C_{1+}) we get the following

constants for first-order side-band:

$$\begin{aligned}
\alpha_1 &= \frac{[(-h_1 + h_2^*)h_5h_6^* + (h_5 - h_6^*)g_{ma}^2](h_4^*h_9 - 2G_{cb_2}^2)G_{mb_1}^2}{(h_1h_5 + g_{ma}^2)(h_2^*h_6^* + g_{ma}^2)}, \\
\alpha_2 &= \frac{[(h_1 - h_2^*)h_5h_6^* + (-h_5 + h_6^*)g_{ma}^2](h_{10}^*h_4^* + 2G_{cb_2}^2)G_{mb_1}^2}{(h_1h_5 + g_{ma}^2)(h_2^*h_6^* + g_{ma}^2)}, \\
\alpha_3 &= \left[h_7 + \left(\frac{2h_5}{h_1h_5 + g_{ma}^2} - \frac{2h_6^*}{h_2^*h_6^* + g_{ma}^2} \right) G_{mb_1}^2 \right], \\
\alpha_4 &= ih_4^*g_{b_1b_2}(h_4^*g_{b_1b_2}^2 + h_7(h_4^*h_9 - G_{cb_2}^2) + \alpha_1), \\
\alpha_5 &= ih_4^*g_{b_1b_2}(h_7G_{cb_2}^2 - \alpha_2), \\
\alpha_6 &= -ih_4^*g_{b_1b_2}(-h_{10}^*h_4^*h_8^*\alpha_4 + h_4^*h_7h_9\alpha_5 \\
&\quad + h_4^*(-\alpha_4 + \alpha_5)g_{b_1b_2}^2 - (h_7 + h_8^*)(\alpha_4 + \alpha_5)G_{cb_2}^2), \\
\alpha_7 &= h_4^{*2}g_{b_1b_2}G_{cb_2} \left(i(h_7 + h_8^*)\alpha_5 + h_4^*g_{b_1b_2}(h_{10}^*h_4^*h_8^* \right. \\
&\quad \left. + h_4^*g_{b_1b_2}^2 + (h_7 + h_8^*)G_{cb_2}^2)\alpha_3 \right), \\
\alpha_8 &= (ih_4^*g_{b_1b_2}(h_{10}^*h_4^*h_8^* + h_4^*g_{b_1b_2}^2 + (h_7 + h_8^*)G_{cb_2}^2))\alpha_6, \\
\alpha_9 &= (ih_4^{*2}(h_7 + h_8^*)g_{b_1b_2}G_{cb_2})\alpha_6 \\
&\quad + (ih_4^*g_{b_1b_2}(h_4^*h_7h_9 + h_4^*g_{b_1b_2}^2 - (h_7 + h_8^*)G_{cb_2}^2))\alpha_7, \\
\alpha_{10} &= \left(\frac{\alpha_7}{\alpha_6} + \frac{\alpha_9}{\alpha_8} \right), \\
\alpha_{11} &= h_3 - G_{cb_2}\alpha_{10}.
\end{aligned}$$

2. Calculations of second-order side-band

The second subgroup exhibits non-linear response (second-order side-band) and described as:

$$\begin{aligned}
M_{2-}l_2 &= ig_{ma}A_{2-} + ig_{mb_1}(M_{1-})(B_{1-} + B_{1+}^*) \\
&\quad - G_{mb_1}(B_{2+}^* + B_{2-}), \\
C_{2+}l_3 &= G_{cb_2}(X_{2-}^* + X_{2+}) + ig_{cb_2}(C_{1+})(X_{1+} + X_{1-}^*), \\
C_{2-}l_4 &= G_{cb_2}(X_{2+}^* + X_{2-}) + ig_{cb_2}(C_{1-})(X_{1-} + X_{1+}^*), \\
A_{2+}l_5 &= -ig_{ma}M_{2+}, \\
A_{2-}l_6 &= -ig_{ma}M_{2-}, \\
B_{2+}l_7 &= ig_{b_1b_2}X_{2+} + ig_{mb_1}(M_{1+}M_{1-}^*) \\
&\quad - G_{mb_1}(M_{2-}^* - M_{2+}), \\
B_{2-}l_8 &= ig_{b_1b_2}X_{2-} + ig_{mb_1}(M_{1-}M_{1+}^*) \\
&\quad - G_{mb_1}(M_{2+}^* - M_{2-}), \\
X_{2+}l_9 &= G_{cb_2}(C_{2-}^* - C_{2+}) - ig_{b_1b_2}B_{2+} \\
&\quad + ig_{cb_2}(C_{1-}^*C_{1+}), \\
X_{2-}l_{10} &= G_{cb_2}(C_{2+}^* - C_{2-}) - ig_{b_1b_2}B_{2-} \\
&\quad - ig_{cb_2}(C_{1+}^*C_{1-}).
\end{aligned} \tag{A2}$$

with $l_1 = 2i\delta - i\tilde{\Delta}_m - \gamma_m$, $l_2 = -2i\delta - i\tilde{\Delta}_m - \gamma_m$, $l_3 = -2i\delta + i\tilde{\Delta}_c + \gamma_c$, $l_4 = 2i\delta + i\tilde{\Delta}_c + \gamma_c$, $l_5 = -2i\delta + i\tilde{\Delta}_a + \gamma_a$, $l_6 = 2i\delta + i\tilde{\Delta}_a + \gamma_a$, $l_7 = 2i\delta - i\omega_{b_1} - \gamma_{b_1}$, $l_8 = -2i\delta - i\omega_{b_1} - \gamma_{b_1}$, $l_9 = -2i\delta + i\omega_{b_2} + \gamma_{b_2}$, and $l_{10} = 2i\delta + i\omega_{b_2} + \gamma_{b_2}$. After solving Eq. (A2) for (C_{2+}) we get the following

constants for second-order side-band:

$$\begin{aligned}
\Psi_1 &= 2ig_{cb_2}G_{cb_2}G_{mb_1}^2 \left(\frac{l_5}{l_1l_5 - g_{ma}^2} + \frac{l_6^*}{-g_{ma}^2 + l_2^*l_6^*} \right), \\
\Psi_2 &= 2ig_{cb_2}G_{mb_1}^2l_4^* \left(\frac{l_5}{l_1l_5 - g_{ma}^2} + \frac{l_6^*}{-g_{ma}^2 + l_2^*l_6^*} \right), \\
\Psi_3 &= \frac{G_{mb_1}^2 (-2G_{cb_2}^2 + l_{10}^*l_4^*) (l_5 (l_1 + l_2^*) l_6^* - g_{ma}^2 (l_5 + l_6^*))}{(l_1l_5 - g_{ma}^2) (g_{ma}^2 - l_2^*l_6^*)}, \\
\Psi_4 &= \frac{G_{mb_1}^2 (2G_{cb_2}^2 + l_9l_4^*) (l_5 (l_1 + l_2^*) l_6^* - g_{ma}^2 (l_5 + l_6^*))}{(l_1l_5 - g_{ma}^2) (g_{ma}^2 - l_2^*l_6^*)}, \\
\Psi_5 &= \frac{l_7G_{cb_2}^2 + (\Psi_3)}{-ig_{b_1b_2} (-2l_7G_{cb_2}^2 + 2g_{b_1b_2}^2l_4^* - l_4^* (G_{cb_2}^2 + l_{10}^*l_4^*) l_8^*)}, \\
\Psi_6 &= -l_7G_{cb_2}^2 + (l_7l_9 - g_{b_1b_2}^2) l_4^* + (\Psi_4) \\
&\quad + i\Psi_5g_{b_1b_2} ((-l_7l_9 + g_{b_1b_2}^2) l_4^* + G_{cb_2}^2 (l_7 + l_4^*l_8^*)), \\
\Psi_7 &= G_{cb_2}L_4^* \left(-l_7 + 2G_{mb_1}^2 \left(\frac{l_5}{l_1l_5 - g_{ma}^2} + \frac{l_6^*}{-g_{ma}^2 + l_2^*l_6^*} \right) \right) \\
&\quad + i\Psi_5g_{b_1b_2} (l_7 + l_4^*l_8^*), \\
\Psi_8 &= -\Psi_1 - \Psi_5g_{b_1b_2}g_{cb_2}G_{cb_2} (l_7 + l_4^*l_8^*), \\
\Psi_9 &= \Psi_2 - g_{cb_2}l_4^* (-il_7 + \Psi_5g_{b_1b_2} (l_7 + l_4^*l_8^*)), \\
\Psi_{10} &= \frac{ig_{b_1b_2} ((-l_7l_9 + g_{b_1b_2}^2)l_4^* + G_{cb_2}^2 (l_7 + l_4^*l_8^*))}{\Psi_6}, \\
\Psi_{11} &= -\Psi_7\Psi_{10} + ig_{b_1b_2}G_{cb_2}l_4^* (l_7 + l_4^*l_8^*), \\
\Psi_{12} &= -\Psi_8\Psi_{10} - g_{b_1b_2}g_{cb_2}G_{cb_2} (l_7 + l_4^*l_8^*), \\
\Psi_{13} &= \Psi_8\Psi_{10} + g_{b_1b_2}g_{cb_2}G_{cb_2} (l_7 + l_4^*l_8^*), \\
\Psi_{14} &= \Psi_9\Psi_{10} - g_{b_1b_2}g_{cb_2}l_4^* (l_7 + l_4^*l_8^*), \\
\Psi_{15} &= \frac{iG_{cb_2}}{g_{b_1b_2} (-2l_7G_{cb_2}^2 + 2g_{b_1b_2}^2l_4^* - l_4^* (G_{cb_2}^2 + l_{10}^*l_4^*) l_8^*)}, \\
\Psi_{16} &= \frac{G_{cb_2}}{\Psi_6}, \\
\Psi_{17} &= l_3 - \Psi_{15}\Psi_{11} - \Psi_{16}\Psi_7, \\
\Psi_{18} &= \Psi_{12}\Psi_{15} + \Psi_{16}\Psi_8, \\
\Psi_{19} &= \Psi_{15}\Psi_{13} - \Psi_{16}\Psi_8, \\
\Psi_{20} &= \Psi_{15}\Psi_{14} + \Psi_{16}\Psi_9, \\
\Psi_{21} &= il_7 (\Psi_{10}\Psi_{15} - \Psi_{16}) g_{cb_2}, \\
\Psi_{22} &= i (\Psi_{10}\Psi_{15} - \Psi_{16}) g_{b_1b_2}g_{mb_1}l_4^*,
\end{aligned}$$

$$\Psi_{23} = \frac{h_5h_6^*\Psi_{22} (h_4 (-h_9\alpha_7\alpha_8 + h_{10}^*\alpha_6\alpha_9) - 2h_4\alpha_6\alpha_8G_{cb_2} + 2(\alpha_7\alpha_8 + \alpha_6\alpha_9) G_{cb_2}^2) G_{mb_1}^2}{(g_{b_1b_2}^2 (h_1h_5 + g_{ma}^2) (h_2^*h_6^* + g_{ma}^2))},$$

$$\Gamma_1 = \frac{\varepsilon_p^2}{h_4^*\alpha_{11}^2\alpha_6^2\alpha_8^2} [h_4 (\alpha_7\alpha_8 + \alpha_6\alpha_9) (ih_4\alpha_6\alpha_8g_{cb_2} + (-\alpha_6\alpha_8\Psi_{20} + \alpha_6\alpha_9 (\Psi_{18} + \Psi_{21}) + \alpha_7\alpha_8 (-\Psi_{19} + \Psi_{21})) G_{cb_2}) + \Psi_{23}].$$

- [1] X. Zhang, C.-L. Zou, L. Jiang, and H. X. Tang, *Sci. Adv.* **2**, e1501286 (2016).
- [2] X. Zuo, Z.-Y. Fan, H. Qian, M.-S. Ding, H. Tan, H. Xiong, and J. Li, *New J. Phys.* **26**, 031201 (2024).
- [3] H. Yuan, Y. Cao, A. Kamra, R. A. Duine, and P. Yan, *Phys. Rep.* **965**, 1 (2022).
- [4] Q.-K. Wan, H.-L. Shi, and X.-W. Guan, *Phys. Rev. B* **109**, L041301 (2024).
- [5] Z. Shen, G.-T. Xu, M. Zhang, Y.-L. Zhang, Y. Wang, C.-Z. Chai, C.-L. Zou, G.-C. Guo, and C.-H. Dong, *Phys. Rev. Lett.* **129**, 243601 (2022).
- [6] X.-L. Hei, X.-L. Dong, J.-Q. Chen, Y.-F. Qiao, X.-F. Pan, X.-Y. Yao, J.-C. Zheng, Y.-M. Ren, X.-W. Huo, and P.-B. Li, *Phys. Rev. Appl.* **22**, 044025 (2024).
- [7] J. W. Rao, S. Kaur, B. M. Yao, E. R. J. Edwards, Y. T. Zhao, X. Fan, D. Xue, T. J. Silva, Y. S. Gui, and C.-M. Hu, *Nat. Commun.* **10**, 2934 (2019).
- [8] T. Wolz, A. Stehli, A. Schneider, I. Boventer, R. Macêdo, A. V. Ustinov, M. Kläui, and M. Weides, *Commun. Phys.* **3**, 3 (2020).
- [9] D. Lachance-Quirion, Y. Tabuchi, A. Gloppe, K. Usami, and Y. Nakamura, *Appl. Phys. Express* **12**, 070101 (2019).
- [10] X. Zhang, *Mater. Today Electron.* **5**, 100044 (2023).
- [11] D. Zhang, X.-M. Wang, T.-F. Li, X.-Q. Luo, W. Wu, F. Nori, and J. You, *npj Quantum Inf.* **1**, 15014 (2015).
- [12] R.-C. Shen, Y.-P. Wang, J. Li, S.-Y. Zhu, G. S. Agarwal, and J. Q. You, *Phys. Rev. Lett.* **127**, 183202 (2021).
- [13] Y. S. Ihn, S.-Y. Lee, D. Kim, S. H. Yim, and Z. Kim, *Phys. Rev. B* **102**, 064418 (2020).
- [14] C.-Z. Chai, Z. Shen, Y.-L. Zhang, H.-Q. Zhao, G.-C. Guo, C.-L. Zou, and C.-H. Dong, *Photon. Res.* **10**, 820 (2022).
- [15] Y.-P. Wang, J. W. Rao, Y. Yang, P.-C. Xu, Y. S. Gui, B. M. Yao, J. Q. You, and C.-M. Hu, *Phys. Rev. Lett.* **123**, 127202 (2019).
- [16] Y. Zhao, J. Rao, Y. Gui, Y. Wang, and C.-M. Hu, *Phys. Rev. Appl.* **14**, 014035 (2020).
- [17] X.-L. Hei, P.-B. Li, X.-F. Pan, and F. Nori, *Phys. Rev. Lett.* **130**, 073602 (2023).
- [18] Z. Zhang, M. O. Scully, and G. S. Agarwal, *Phys. Rev. Res.* **1**, 023021 (2019).
- [19] J. M. P. Nair and G. S. Agarwal, *Appl. Phys. Lett.* **117**, 084001 (2020).
- [20] S. P. Wolski, D. Lachance-Quirion, Y. Tabuchi, S. Kono, A. Noguchi, K. Usami, and Y. Nakamura, *Phys. Rev. Lett.* **125**, 117701 (2020).
- [21] D. Lachance-Quirion, S. P. Wolski, Y. Tabuchi, S. Kono, K. Usami, and Y. Nakamura, *Science* **367**, 425 (2020).
- [22] M. S. Ebrahimi, A. Motazedifard, and M. B. Harouni, *Phys. Rev. A* **103**, 062605 (2021).
- [23] C. Kittel, *Phys. Rev.* **110**, 836 (1958).
- [24] Y. Tabuchi, S. Ishino, T. Ishikawa, R. Yamazaki, K. Usami, and Y. Nakamura, *Phys. Rev. Lett.* **113**, 083603 (2014).
- [25] D. Hatanaka, M. Asano, H. Okamoto, Y. Kunihashi, H. Sanada, and H. Yamaguchi, *Phys. Rev. Appl.* **17**, 034024 (2022).
- [26] T.-X. Lu, H. Zhang, Q. Zhang, and H. Jing, *Phys. Rev. A* **103**, 063708 (2021).
- [27] A. Kani, B. Sarma, and J. Twamley, *Phys. Rev. Lett.* **128**, 013602 (2022).
- [28] S.-N. Huai, Y.-L. Liu, J. Zhang, L. Yang, and Y.-x. Liu, *Phys. Rev. A* **99**, 043803 (2019).
- [29] Q. Guo, J. Cheng, H. Tan, and J. Li, *Phys. Rev. A* **108**, 063703 (2023).
- [30] J. Li and S. Gröblacher, *Quantum Sci. Technol.* **6**, 024005 (2021).
- [31] Y.-T. Chen, L. Du, Y. Zhang, and J.-H. Wu, *Phys. Rev. A* **103**, 053712 (2021).
- [32] H. Xiong, *Appl. Phys. Lett.* **124**, 112403 (2024).
- [33] C. A. Potts, E. Varga, V. A. S. V. Bittencourt, S. V. Kusminskiy, and J. P. Davis, *Phys. Rev. X* **11**, 031053 (2021).
- [34] R.-C. Shen, J. Li, Z.-Y. Fan, Y.-P. Wang, and J. Q. You, *Phys. Rev. Lett.* **129**, 123601 (2022).
- [35] S. Bayati, M. B. Harouni, and A. Mahdifar, *Opt. Express* **32**, 14914 (2024).
- [36] M. Aspelmeyer, T. J. Kippenberg, and F. Marquardt, *Rev. Mod. Phys.* **86**, 1391 (2014).
- [37] J. Zhao, L. Wu, T. Li, Y.-x. Liu, F. Nori, Y. Liu, and J. Du, *Phys. Rev. Appl.* **15**, 024056 (2021).
- [38] C. Kong, B. Wang, Z.-X. Liu, H. Xiong, and Y. Wu, *Opt. Express* **27**, 5544 (2019).
- [39] Y.-P. Wang, G.-Q. Zhang, D. Zhang, T.-F. Li, C.-M. Hu, and J. Q. You, *Phys. Rev. Lett.* **120**, 057202 (2018).
- [40] B. Wang, Z.-X. Liu, C. Kong, H. Xiong, and Y. Wu, *Opt. Express* **26**, 20248 (2018).
- [41] X. Li, X. Wang, Z. Wu, W.-X. Yang, and A. Chen, *Phys. Rev. B* **104**, 224434 (2021).
- [42] A. Wahab, M. Abbas, X. Yang, and Y. Chen, *Chaos Solitons Fractals* **187**, 115436 (2024).
- [43] X.-H. Lu, L.-G. Si, X.-Y. Wang, and Y. Wu, *Opt. Express* **29**, 4875 (2021).
- [44] G.-T. Xu, M. Zhang, Y. Wang, Z. Shen, G.-C. Guo, and C.-H. Dong, *Phys. Rev. Lett.* **131**, 243601 (2023).
- [45] Q. Wu, H.-J. Sun, Y.-D. Chen, and Z.-X. Liu, *Phys. Rev. A* **110**, 023507 (2024).
- [46] H. Hodaie, A. U. Hassan, S. Wittek, H. Garcia-Gracia, R. El-Ganainy, D. N. Christodoulides, and M. Khajavikhan, *Nature* **548**, 187 (2017).
- [47] H. Xiong, L.-G. Si, A.-S. Zheng, X. Yang, and Y. Wu, *Phys. Rev. A* **86**, 013815 (2012).
- [48] S. A. Diddams, K. Vahala, and T. Udem, *Science* **369**, eaay3676 (2020).
- [49] M.-A. Miri, G. D'Aguanno, and A. Alù, *New J. Phys.* **20**, 043013 (2018).
- [50] Z.-X. Liu and Y.-Q. Li, *Photon. Res.* **10**, 2786 (2022).
- [51] Z. Wang, H. Y. Yuan, Y. Cao, Z.-X. Li, R. A. Duine, and P. Yan, *Phys. Rev. Lett.* **127**, 037202 (2021).
- [52] T. Hula, K. Schultheiss, F. J. T. Gonçalves, L. Körber, M. Bejarano, M. Copus, L. Flacke, L. Liensberger, A. Buzdakov, A. Kákay, M. Weiler, R. Camley, J. Fassbender, and H. Schultheiss, *Appl. Phys. Lett.* **121**, 112404 (2022).
- [53] T. Udem, R. Holzwarth, and T. W. Hänsch, *Nature* **416**, 233 (2002).
- [54] Y.-F. Jiao, T.-X. Lu, and H. Jing, *Phys. Rev. A* **97**, 013843 (2018).
- [55] J.-H. Liu, Y.-F. Yu, Q. Wu, J.-D. Wang, and Z.-M. Zhang, *Opt. Express* **29**, 12266 (2021).
- [56] L.-Y. He, *Phys. Rev. A* **99**, 033843 (2019).
- [57] B. Chen, L. Shang, X.-F. Wang, J.-B. Chen, H.-B. Xue,

- X. Liu, and J. Zhang, *Phys. Rev. A* **99**, 063810 (2019).
- [58] W.-L. Xu, Y.-P. Gao, T.-J. Wang, and C. Wang, *Opt. Express* **28**, 22334 (2020).
- [59] C. Zhao, Z. Yang, R. Peng, J. Yang, C. Li, and L. Zhou, *Phys. Rev. Appl.* **18**, 044074 (2022).
- [60] V. A. S. V. Bittencourt, I. Liberal, and S. Viola Kusminskiy, *Phys. Rev. Lett.* **128**, 183603 (2022).
- [61] C. Potts, V. Bittencourt, S. V. Kusminskiy, and J. Davis, *Phys. Rev. Appl.* **13**, 064001 (2020).
- [62] W. Zhang and H. Z. Shen, *Phys. Rev. A* **109**, 033701 (2024).
- [63] T.-X. Lu, X. Xiao, L.-S. Chen, Q. Zhang, and H. Jing, *Phys. Rev. A* **107**, 063714 (2023).
- [64] K. Ullah, M. T. Naseem, and O. E. Müstecaplıoğlu, *Phys. Rev. A* **102**, 033721 (2020).
- [65] S. Das, S. Chakraborty, and T. N. Dey, *Phys. Rev. A* **108**, 033517 (2023).
- [66] Z.-X. Liu, H. Xiong, and Y. Wu, *IEEE Access* **7**, 57047 (2019).
- [67] Z.-L. Feng and M. Yin, *Phys. Lett. A* **421**, 127781 (2022).
- [68] F. Zimmer and M. Fleischhauer, *Phys. Rev. Lett.* **92**, 253201 (2004).
- [69] M. S. Shahriar, G. S. Pati, R. Tripathi, V. Gopal, M. Messall, and K. Salit, *Phys. Rev. A* **75**, 053807 (2007).
- [70] V. Fiore, Y. Yang, M. C. Kuzyk, R. Barbour, L. Tian, and H. Wang, *Phys. Rev. Lett.* **107**, 133601 (2011).
- [71] J. Li, S.-Y. Zhu, and G. S. Agarwal, *Phys. Rev. Lett.* **121**, 203601 (2018).
- [72] H. Huebl, C. W. Zollitsch, J. Lotze, F. Hocke, M. Greifenstein, A. Marx, R. Gross, and S. T. B. Goennenwein, *Phys. Rev. Lett.* **111**, 127003 (2013).
- [73] X. Zhang, C.-L. Zou, L. Jiang, and H. X. Tang, *Phys. Rev. Lett.* **113**, 156401 (2014).
- [74] M. Yu, H. Shen, and J. Li, *Phys. Rev. Lett.* **124**, 213604 (2020).
- [75] Z.-X. Su, A.-D. Zhu, and L. Yu, *Phys. Rev. A* **110**, 023502 (2024).
- [76] H. Suzuki, E. Brown, and R. Sterling, *Phys. Rev. A* **92**, 033823 (2015).
- [77] S. Weis, R. Rivière, S. Deléglise, E. Gavartin, O. Arcizet, A. Schliesser, and T. J. Kippenberg, *Science* **330**, 1520 (2010).
- [78] T.-X. Lu, Y.-F. Jiao, H.-L. Zhang, F. Saif, and H. Jing, *Phys. Rev. A* **100**, 013813 (2019).
- [79] H. Lü, C. Wang, L. Yang, and H. Jing, *Phys. Rev. Appl.* **10**, 014006 (2018).
- [80] C. W. Gardiner and M. J. Collett, *Phys. Rev. A* **31**, 3761 (1985).
- [81] L. Li, W.-X. Yang, Y. Zhang, T. Shui, A.-X. Chen, and Z. Jiang, *Phys. Rev. A* **98**, 063840 (2018).
- [82] K. Qu and G. S. Agarwal, *Phys. Rev. A* **87**, 063813 (2013).
- [83] K. Ullah, H. Jing, and F. Saif, *Phys. Rev. A* **97**, 033812 (2018).
- [84] H. Xiong, L.-G. Si, and Y. Wu, *Appl. Phys. Lett.* **110**, 171102 (2017).
- [85] D.-G. Lai, X. Wang, W. Qin, B.-P. Hou, F. Nori, and J.-Q. Liao, *Phys. Rev. A* **102**, 023707 (2020).
- [86] C. Kong, H. Xiong, and Y. Wu, *Phys. Rev. A* **95**, 033820 (2017).
- [87] H. Xiong, Z.-X. Liu, and Y. Wu, *Opt. Lett.* **42**, 3630 (2017).
- [88] K. Børkje, A. Nunnenkamp, J. D. Teufel, and S. M. Girvin, *Phys. Rev. Lett.* **111**, 053603 (2013).
- [89] H.-J. Chen, *Opt. Laser Technol.* **161**, 109242 (2023).
- [90] X.-W. Xu and Y. Li, *Phys. Rev. A* **92**, 023855 (2015).
- [91] L. J. Wang, A. Kuzmich, and A. Dogariu, *Nature* **406**, 277 (2000).
- [92] W. Z. Jia, L. F. Wei, Y. Li, and Y.-x. Liu, *Phys. Rev. A* **91**, 043843 (2015).
- [93] Y. Li, Y. Y. Huang, X. Z. Zhang, and L. Tian, *Opt. Express* **25**, 18907 (2017).